PROCEEDINGS, 43nd Workshop on Geothermal Reservoir Engineering
Stanford University, Stanford, California, February 12-14, 2018
SGP-TR-213

Analysis of a Long-Term Test by Inverse Modeling Surface Deformation as Measured by InSAR

John Akerley[1], Sam Batzli[2], Michael A. Cardiff[2], Patrick Walsh[1], and Kurt L. Feigl[2]

[1]Ormat Nevada Inc.., Reno, Nevada; [2]Department of Geoscience, University of Wisconsin-Madison, Madison, Wisconsin

jakerley@ORMAT.COM, pwalsh@ormat.com, sabatzli@wisc.edu, cardiff@wisc.edu, feigl@wisc.edu

Keywords: InSAR, subsurface characterization

ABSTRACT

Following the completion of a production well and an injection well at an undeveloped geothermal field in Nevada, a long-term flow test was conducted to measure and understand reservoir characteristics. Measurements were made several times daily of variables including: volumetric flow rate of injection, volumetric flow rate of production, downhole pressure in production wells and wellhead pressure in the injection well. To better understand reservoir flow paths, a chemical tracer was also injected in the injection well. To measure the deformation, we use Interferometric Synthetic Aperture Radar (InSAR). Interferometric pairs of SAR images acquired every 11 days during the test show uplift around the injection well. To interpret the deformation field, we perform inverse modeling using the General Inversion of Phase Technique (GIPhT). This study demonstrates the value of combining InSAR data with conventional data to constrain models of reservoir characteristics and rock properties. For example, the modeled volume change estimated from the InSAR data is comparable to the value measured at the wellhead. Similarly, by matching the modeled pressure value to the measured value, we expect to be able to constrain the bulk modulus at the field scale.

The work presented herein was funded in part by the Office of Energy Efficiency and Renewable Energy (EERE), U.S. Department of Energy, under Award Number DE-EE0006760.

1. INTRODUCTION

Long-term, multi-well field tests are a valuable tool in understanding reservoir characteristics and evaluating the potential success of full-field development. The goal of the test is to gain insight into the reservoir by producing and injecting to create a noticeable reservoir pressure drawdown. The exploration and development program for an undeveloped geothermal field utilizes the following steps [*DiPippo*, 2012]:

1. Literature survey
2. Airborne survey
3. Geologic survey
4. Hydrologic survey
5. Geochemical survey
6. Geophysical survey
7. Exploration drilling
    a. Corehole drilling
    b. Full size drilling
    c. Completion testing
8. Multi-well testing
9. Reservoir modeling and analysis
10. Project construction release
11. Development drilling.

Iterations in refining the geologic analysis and conceptual model continue throughout the process as testing and evaluations continue to raise new questions.

The study area for the current work is an undeveloped geothermal field in Nevada that includes a production well and an injection well. The test was designed to run for a maximum of two months. Measurements were made several times daily of variables including: volumetric flow rate of injection, volumetric flow rate of production, downhole pressure in the production well, wellhead pressure in the injection well, and downhole pressure in four monitoring wells. To better understand reservoir flow paths, a chemical tracer was also injected in the injection well and sampled daily in the production well. In an attempt to view deformation due to pressure changes and injection-induced formation cooling, Synthetic Aperture Radar (SAR) images were acquired every eleven days during the test.

2. WELL TEST PROCEDURE

A test procedure and duration were planned based on the short drilling completion tests and the desired results of the long-term test.

As seen in Figure 1, a flow test facility was designed to bring single-phase fluid to the surface, flash at atmospheric pressure, and then inject into a nearby well. A 12-stage downhole lineshaft pump powered by a 400-horsepower motor was installed in the production well to produce a maximum of 2000 gallons per minute (gpm). The production rate was managed with a throttle valve to adjust the discharge pressure. The atmospheric flash vessel cooled the produced fluid to below boiling, and water storage tanks were filled to effectively maintain injection as well as allow for momentary failures of equipment. Brine was pumped from the production well pad to the injection well pad and then pressure was increased in inject into the injection well. Equipment was monitored at all times for the duration of the test, and readings were recorded four times daily.

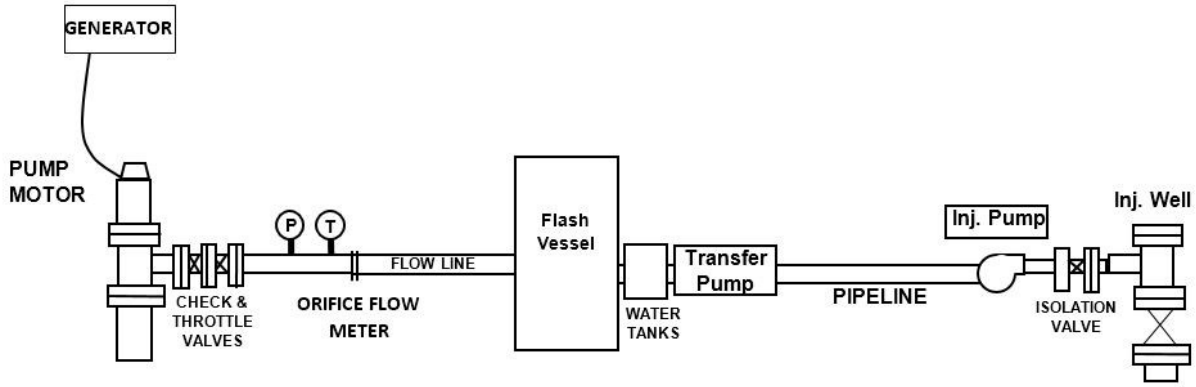

Figure 1. Test facility at the production and injection well.

A chemical tracer, 2-Napthalene Sulfonate, totaling 50 kg was injected after equipment was proven functional and readings stabilized. Production fluid was sampled once daily to measure returns and infer reservoir connectivity.

Pressure changes due to pumping and injecting were observed at four locations with proximities to the production and injection wells outlined in Table 1.

Table 1. Distance from monitoring wells (MW) to the production well (PW) and injection well (IW).

	Distance to PW [m]	Distance to IW [m]
MW 1	35	373
MW 2	873	547
MW 3	2120	2309
MW 4	346	6

3. RESULTS AND DISCUSSION

3.1 Flow test

The long-term test was run for 46 days prior to shutting in the production well. The average flow rate was 1600 gpm, and the average injection rate was about 1350 gpm, variance due mostly to a difference in fluid density at constant mass flow rate. The estimated total volume injected was 90,861,600 gallons at an average 185°F temperature. The wellhead pressure in the injection well increased during that time in a manner approximating radial flow in an infinite planar aquifer. Figure 2 shows a radial flow pressure calculation matched to the pressure increase observed at the injection wellhead and then projected to one year. Injection at 1347 gpm reaches 370 psig wellhead pressure in one year.

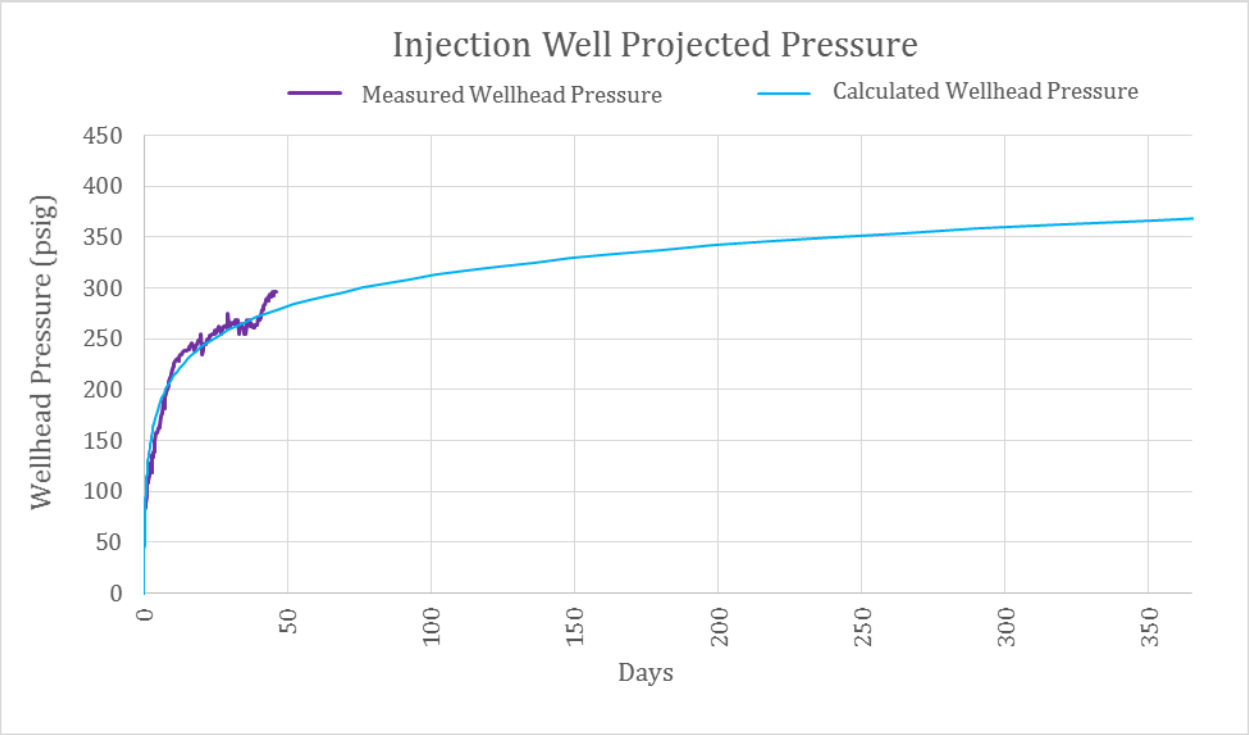

Figure 2. Projected wellhead pressure for the injection well using radial flow model.

Figure 3 shows the monitor well data from the four downhole measurements for the duration of the test. In Monitor Well 2 and Monitor Well 3, the nitrogen leaked in the first several days of the test so the tubing was replaced. A modest drawdown of about 3 psi was seen near the production well that recovered as the production rate was decreased from an initial 2000 gpm. There was no noticeable change in the downhole pressure near the injection well nor in the two monitor wells at greater distance.

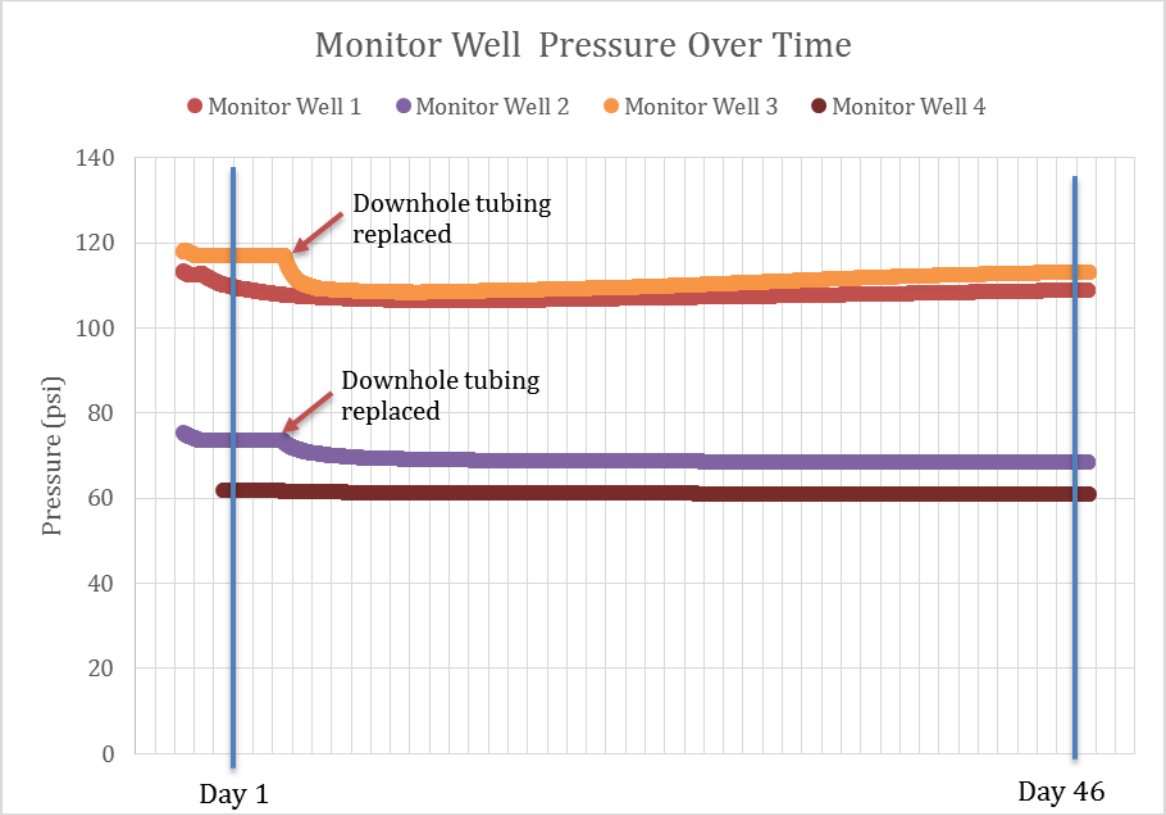

Figure 3. Time series of pressure records showing the response to production and injection. For interpretation, a change of 10 psi of pressure corresponds to change in water level of the order of 23 feet.

The tracer returns measured in the production well totaled 0.04 kg at the completion of the test. Based on the mass return percentage, the total percent of production fluid from injection is 0.07 percent.

3.2 Remote sensing

As described elsewhere [e.g., *Massonnet and Feigl*, 1998], interferometric analysis of synthetic aperture radar images (InSAR) is a geodetic technique that calculates the interference pattern caused by the difference in phase between two images acquired by a satellite radar sensor at two distinct times. The resulting interferogram is a contour map of the change in distance between the ground and the radar instrument. These maps provide a spatial sampling density of ~100 pixels/km^2, a precision of ~10 mm, a registration accuracy of ~10 m, and an observation cadence of ~1 pass/week. This remote-sensing tool has been demonstrated and validated for many actively deforming areas, including the geothermal fields at East Mesa, California and Brady Hot Springs, Nevada [e.g., *Massonnet et al.*, 1997; *Massonnet et al.*, 1998; *Oppliger et al.*, 2004; *Han et al.*, 2011; *Trugman et al.*, 2014; *Ali et al.*, 2016; *Reinisch et al.*, 2016a; *Feigl and PoroTomo_Team*, 2017].

The geodetic data set includes several SAR images covering the study area. The X-band SAR sensor aboard the TerraSAR-X [*Pitz and Miller*, 2010] mission operated by the German Space Agency (DLR) acquired images on several dates before, during, and after the flow test.

We combine the SAR images into interferometric combinations (interferograms). To generate the interferograms, we use the GMTSAR InSAR processing software [*Sandwell et al.*, 2011]. The wrapped phase values are filtered using their two-dimensional spectra [*Goldstein and Werner*, 1998]. As in previous studies [e.g., *Feigl et al.*, 2014], we do not unwrap the phase values at all.

The observed values of wrapped phase change for an 88-day time interval including the flow test appear in the first panel (a) of Figure 4. The principal signal in the interferograms is a concentric fringe pattern centered near the injection well. The range from satellite to ground decreases with time, consistent with uplift. In this interferogram, one fringe of phase change corresponds to 15.5 mm of range change along the line of sight between the satellite and the ground at an incidence angle of 27° from vertical. The single fringe indicates more than 15 mm of range change over the 88-day measurement interval. If the motion were purely vertical, then the maximum rate of uplift $\partial u_z/\partial t$ would be approximately 65 mm/yr or 177 μm/day.

The individual SAR images combine to form eight useful pair-wise interferograms. In terms of graph theory, the epochs correspond to vertices on a graph and the pairs to edges [*Reinisch et al.*, 2016b]. The graph for the InSAR data set includes three separate trees, each of which is an acyclic and connected graph.

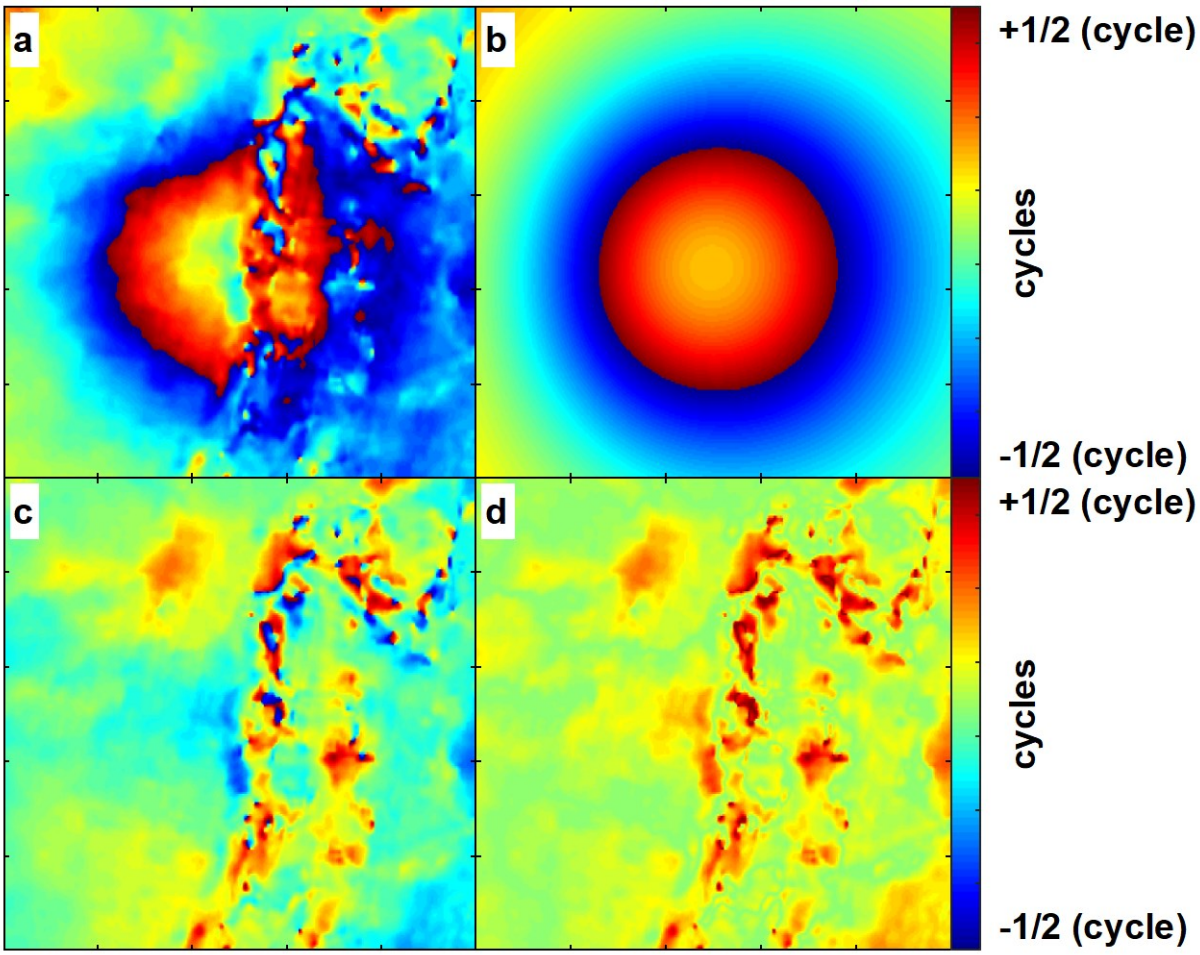

Figure 4. SAR interferograms for interferometric pair, spanning the 88-day time interval. The panels include (a) observed phase values; (b) modeled phase values calculated from the final estimate of the parameters in the Okada dislocation model; (c) final residual phase values formed by subtracting final modeled values from observed phase values; and (d) angular deviations for final estimate. One cycle of phase denotes 15.5 mm of range change. Tick marks denote 500-meter grid in easting and northing.

To interpret the observed deformation field, we imagine that the injected fluids flow into a shallow volume of soft sedimentary and alluvial material. In this conceptual model, the deep layers are composed of stiffer material that is much less permeable. As a result, the injected fluid inflates a shallow source located around the open interval of the injection well, as sketched in Figure 5. The inflating shallow source produces uplift at the ground surface.

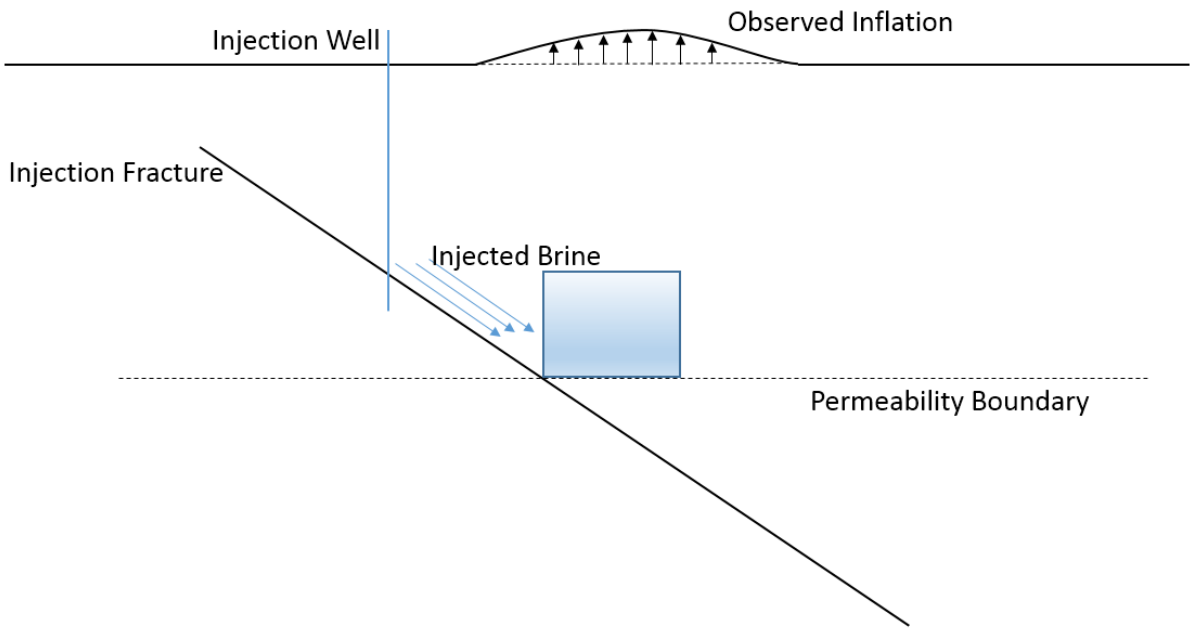

Figure 5. Sketch of conceptual model in vertical cross section, showing the key idea that the injected fluid increases the volume of the permeable shallow rock layers because it cannot flow into the basement rocks with low permeability.

3.3 Mechanical modeling

To simulate the observed deformation field, we use the General Inversion of Phase Technique (GIPhT) as developed by Feigl and Thurber (2009). The source code for GIPhT is written in Matlab and freely available at https://github.com/feigl/gipht. In this case, the model includes a cubic source composed of three mutually orthogonal, square dislocations embedded in a half space with uniform elastic properties [*Okada*, 1985]. This calculation has been validated against other analytic solutions [*Mindlin and Cheng*, 1950a; *Mindlin and Cheng*, 1950b; *Mogi*, 1958], as described elsewhere [*Bonafede and Ferrari*, 2009]. For a cubic source with a width of W = 100 m, a centroid depth of $-Z$ = 100 m, and volume change of ΔV = 60 m^3, the modeled displacement field $\mathbf{U}$ calculated at the surface agrees within less than 60 μm in all three components [Reinisch, in prep.].

In our case, we assume a Poisson's ratio ν = 0.15. For each InSAR pair, we estimate a set of adjustable model parameters including geophysical parameters related to the time interval and nuisance parameters related to the acquisition epochs of the first and second SAR images. The geophysical parameters include the three-dimensional centroid coordinates (X_c, Y_c, Z_c) of the cubic source and its rate of volumetric change $\dot{V}$. The nuisance parameters include an additive phase offset and three components of the phase gradient over the entire interferogram. The estimated rate of volume change, in m^3/year, for each pair is shown in Figure 6.

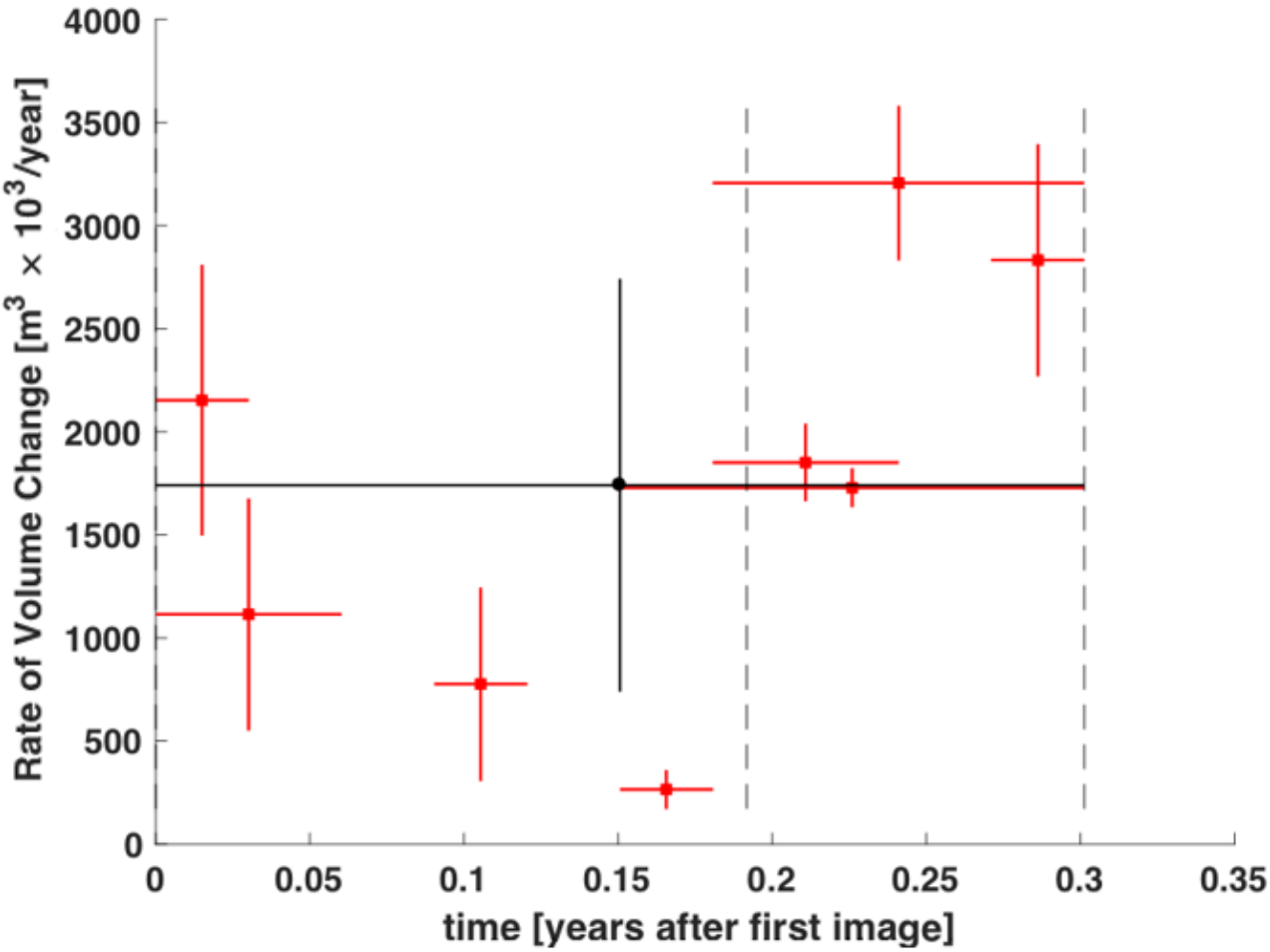

Figure 6. Rates of net volume change estimated from InSAR pairs using single cube model. Each vertical bar represents the 68 percent confidence interval for the estimated volume change. Each horizontal bar indicates the time interval spanned by the corresponding interferometric pair. The start and end of the dataset as well as the start of the flow test are denoted with black dashed lines.

In order to evaluate the time dependence, we perform time-series analysis using temporal adjustment [*Reinisch et al.,* 2016b]. This procedure converts the rate of volume change estimated over several time intervals into the integrated volume at each point in time [*Ali et al*, 2016]. The result in Figure 7 shows a modeled linear increase in volume rate change of 58.5 ± 9 x 10^{-3} m^3/s for a total volume change of 233 ± 40 x 10^3 m^3 at the end of the test.

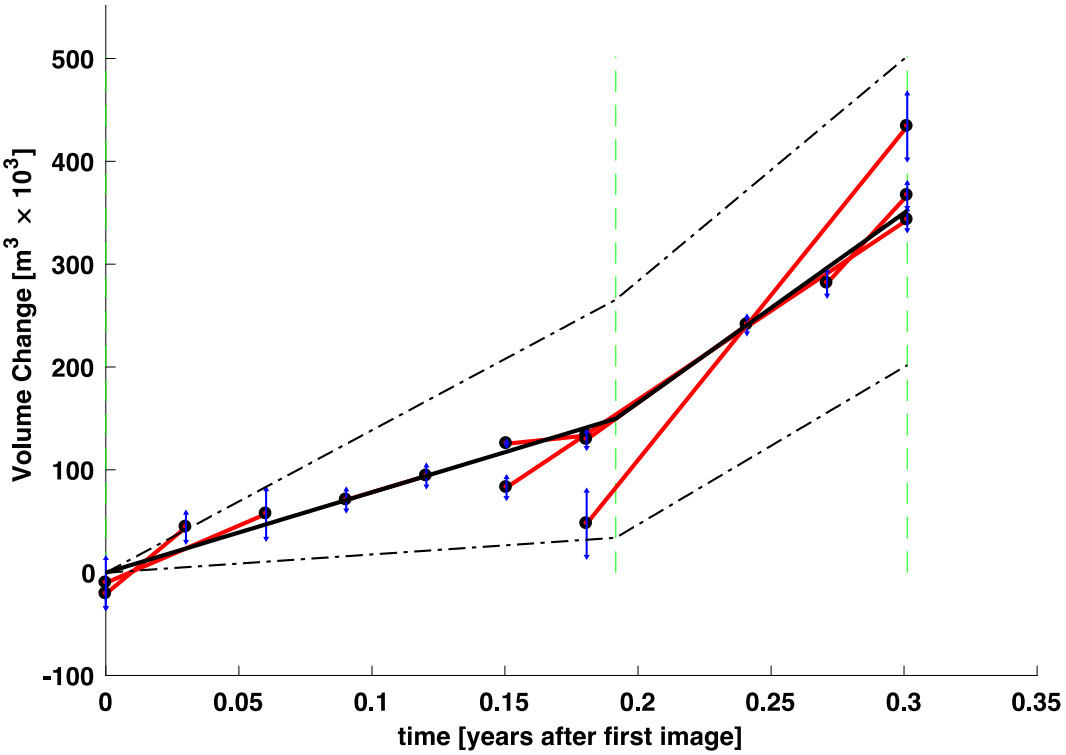

Figure 7. Volume change as a function of time. The black line shows a model estimated by the temporal adjustment procedure [*Reinisch et al.*, 2016b]. The model is parameterized as piecewise-linear polynomial with two segments. Pair-wise estimates of volume changes derived from InSAR measurements are indicated in red, with 1-sigma uncertainties denoted in blue. Modeled displacement is shown by the solid black line, with upper and lower uncertainties denoted with dashed black lines. The start and end of the dataset as well as the start of the flow test are denoted with green dashed lines.

4. CONCLUSIONS

A long-term multi-well test was run for 46 days at an undeveloped geothermal field in Nevada with a production well averaging 1600 gpm and an injection well taking 1350 gpm. The injection well immediately began to pressurize exhibiting a behavior approximated by radial flow in an infinite planar aquifer.

The volume change (of the elastic medium at depth) estimated from InSAR is lower than the volume change measured by Ormat (at the surface) by a factor of 0.7. This difference could be attributed to one or a combination of several factors. First, it's not expected that 100% of the injected fluid would remain in the shallow zone. Though the tracer showed only a very small percentage of injection return to production, the results confirmed that a positive percentage of injection does cross the permeability barrier shown in Figure 5. Another possibility is the combination of inflation due to volume change and thermal contraction of the rock at the injected depth where the reservoir is hotter than the injection temperature. Other possible explanations include shape of subsurface inflation and reservoir bulk rock properties. Future work on this and other geothermal fields will attempt to model thermomechanical effects.

ACKNOWLEDGMENTS

SAR data from the TerraSAR-X and TanDEM-X satellite missions operated by the German Space Agency (DLR) were acquired from Airbus under a contract.

The work presented herein was funded in part by the Office of Energy Efficiency and Renewable Energy (EERE), U.S. Department of Energy, under Award Numbers DE-EE0006760.

REFERENCES

Ali, S. T., J. Akerley, E. C. Baluyut, M. Cardiff, N. C. Davatzes, K. L. Feigl, W. Foxall, D. Fratta, R. J. Mellors, P. Spielman, H. F. Wang, and E. Zemach (2016), Time-series analysis of surface deformation at Brady Hot Springs geothermal field (Nevada) using interferometric synthetic aperture radar, *Geothermics, 61*, 114-120. http://dx.doi.org/10.1016/j.geothermics.2016.01.008

Bonafede, M., and C. Ferrari (2009), Analytical models of deformation and residual gravity changes due to a Mogi source in a viscoelastic medium, *Tectonophysics, 471*, 4-13. http://dx.doi.org/10.1016/j.tecto.2008.10.006

DiPippo, Ronald. *Geothermal Power Plants: Principles, Applications and Case Studies*. 3rd ed., Elsevier, BH, 2012.

Feigl, K. L., H. Le Mével, S. Tabrez Ali, L. Córdova, N. L. Andersen, C. DeMets, and B. S. Singer (2014), Rapid uplift in Laguna del Maule volcanic field of the Andean Southern Volcanic zone (Chile) 2007–2012, *Geophys. J. Int., 196*, 885-901. http://dx.doi.org/10.1093/gji/ggt438

Feigl, K. L., and PoroTomo_Team (Year), Overview and Preliminary Results from the PoroTomo Project at Brady Hot Springs, Nevada: Poroelastic Tomography by Adjoint Inverse Modeling of Data from Seismology, Geodesy, and Hydrology, paper presented at Stanford Geothermal Workshop, Stanford University. https://pangea.stanford.edu/ERE/db/GeoConf/papers/SGW/2017/Feigl.pdf

Goldstein, R. M., and C. L. Werner (1998), Radar interferogram filtering for geophysical applications, *Geophys. Res. Lett., 25*, 4035-4038.

Han, J.-Y., R. R. Forster, D. E. Moser, A. L. J. Ford, J. Ramirez-Hernandez, and K. F. Tiampo (2011), The spatial and temporal subsidence variability of the East Mesa Geothermal Field, California, USA, and its potential impact on the All American Canal System, *International Journal of Remote Sensing, 32*, 3427-3449. http://dx.doi.org/10.1080/01431161003749444

Massonnet, D., T. Holzer, and H. Vadon (1997), Land subsidence caused by the East Mesa geothermal field, California, observed using SAR interferometry, *Geophys. Res. Lett., 24*, 901-904.

Massonnet, D., and K. L. Feigl (1998), Radar interferometry and its application to changes in the Earth's surface, *Rev. Geophys., 36*, 441-500. http://dx.doi.org/10.1029/97RG03139

Massonnet, D., T. Holzer, and H. Vadon (1998), Correction to "Land subsidence caused by the East Mesa geothermal field, California, observed using SAR interferometry", *Geophys. Res. Lett., 25*, 3213-3213.

Mindlin, R. D., and D. H. Cheng (1950a), Thermoelastic Stress in the Semi-Infinite Solid, *Journal of Applied Physics, 21*, 931.

Mindlin, R. D., and D. H. Cheng (1950b), Nuclei of Strain in the Semi-Infinite Solid, *Journal of Applied Physics, 21*, 926.

Mogi, K. (1958), Relations between the eruption of various volcanoes and the deformations of the ground surfaces around them, *Bull. Earthquake Research Institute, 36*, 99-134.

Okada, Y. (1985), Surface deformation due to shear and tensile faults in a half-space, *Bulletin of the Seismological Society of America, 75*, 1135-1154. http://www.bssaonline.org/content/75/4/1135.abstract

Oppliger, G., M. Coolbaugh, and W. Foxall (2004), Imaging structure with fluid fluxes at the Bradys geothermal field with satellite interferometric radar (InSAR): New insights into reservoir extent and structural controls, *Geothermal Resources Council Transactions, 28*, 37-40. http://unr.edu/geothermal/pdffiles/OppligerCoolbaughFoxallGRC04.pdf

Pitz, W., and D. Miller (2010), The TerraSAR-X Satellite, *Geoscience and Remote Sensing, IEEE Transactions on, 48*, 615-622. http://dx.doi.org/10.1109/TGRS.2009.2037432

Reinisch, E. C., S. T. Ali, M. Cardiff, C. Kreemer, P. Team, and K. L. Feigl (2016a of Conference), Analysis of Interferometric Synthetic Aperture Radar Phase Data at Brady Hot Springs, Nevada, USA Using Prior Information (abstract #NS41A-1899), abstract presented at Fall Meeting American Geophysical Union, San Francisco. https://agu.confex.com/agu/fm16/meetingapp.cgi/Paper/134641

Reinisch, E. C., M. Cardiff, and K. L. Feigl (2016b), Graph theory for analyzing pair-wise data: application to geophysical model parameters estimated from interferometric synthetic aperture radar data at Okmok volcano, Alaska, *J Geod*, 1-16. http://dx.doi.org/10.1007/s00190-016-0934-5

Sandwell, D., R. Mellors, X. Tong, M. Wei, and P. Wessel (2011), Open radar interferometry software for mapping surface deformation, *Eos, Transactions American Geophysical Union, 92*, 234-234. http://topex.ucsd.edu/gmtsar

Trugman, D. T., A. A. Borsa, and D. T. Sandwell (2014), Did stresses from the Cerro Prieto Geothermal Field influence the El Mayor-Cucapah rupture sequence?, *Geophysical Research Letters, 41*, 8767-8774. http://dx.doi.org/10.1002/2014GL061959